Energy & Environmental Science

Accepted Manuscript

ROYAL SOCIETY OF CHEMISTRY

www.rsc.org/ees

Peanut Shell Hybrid Sodium Ion Capacitor with Extreme Energy - Power Rivals Lithium Ion Capacitors

Jia Ding[a,b], *Huanlei Wang*[a,b], *Zhi Li*[a,b*], *Kai Cui*[b], *Dimitre Karpuzov*[c], *Xuehai Tan*[a,b], *Alireza Kohandehghan*[a,b], *David Mitlin*[a,b,d**]

[a] Chemical and Materials Engineering, University of Alberta, Edmonton, Alberta T6G 2V4, Canada

[b] National Institute for Nanotechnology (NINT), National Research Council of Canada, Edmonton, Alberta T6G 2M9, Canada

[c] University of Alberta, Alberta Centre for Surface Engineering and Science, Edmonton, Canada

[d] Chemical & Biomolecular Engineering , Clarkson University
8 Clarkson Ave., Potsdam, New York 13699, USA

* lizhicn@gmail.com, **david.mitlin2@gmail.com

ABSTRACT: This is the first report of a hybrid sodium ion capacitor (NIC) with the active materials in *both* the anode and the cathode being derived entirely from a single precursor: peanut shells, which are a green and highly economical waste globally generated at over 6 million tons per year. The electrodes push the envelope of performance, delivering among the most promising sodiation capacity - rate capability - cycling retention combinations reported in literature for each materials class. Hence the resultant NIC also offers a state-of-the-art cyclically stable combination of energy and power, not only in respect to previously published NICs but also as compared to Li ion capacitors (LICs). The ion adsorption cathode based on Peanut Shell Nanosheet Carbon (PSNC) displays a hierarchically porous architecture, a sheet-like morphology down to 15 nm in thickness, a surface area on par with graphene materials (up to 2396 m^2g^{-1}) and high levels of oxygen doping (up to 13.51 wt%). Scanned from 1.5 - 4.2 V *vs*. Na/Na^+ PSNC delivers a specific capacity of 161 $mAhg^{-1}$ at 0.1A g^{-1} and 73 $mAhg^{-1}$ at 25.6 Ag^{-1}. A low surface area Peanut Shell Ordered Carbon (PSOC) is employed as an ion intercalation anode. PSOC delivers a total capacity of 315 $mAhg^{-1}$ with a flat plateau of 181 $mAhg^{-1}$ occurring below 0.1 V (tested at 0.1 Ag^{-1}), and is stable at 10,000 cycles (tested at 3.2 Ag^{-1}). The assembled NIC operates within a wide temperature range (0 - 65°C), yielding at room temperature (by active mass) 201, 76 and 50 Wh kg^{-1} at 285, 8500 and 16500 W kg^{-1}, respectively. At 1.5 - 3.5 V, the hybrid device achieved 72% capacity retention after 10,000 cycles tested at 6.4 Ag^{-1}, and 88% after 100,000 cycles at 51.2 Ag^{-1}.

KEYWORDS: Na ion capacitor, Li ion capacitor, battery, graphene, NIB, NAB, SIB, LIB

Electrical energy storage (EES) systems play a crucial role in consumer electronics, automotive, aerospace and stationary markets. Due to sodium's effectively inexhaustible and democratically distributed reserves, Na - ion based energy storage devices are a promising alternative to the well-developed Li - ion technologies.[1,2,3,4,5,6,7,8,9,10,11,12,13,14,15,16] There are primarily two types of devices for energy storage; batteries *e.g.* [17, 18, 19, 20, 21] and electrochemical capacitors *e.g.*[22,23,24,25,26,27,28,29,30,31,32,33,34]. The former offers a high energy density while the later offers high power. For instance, commercial lithium ion batteries deliver a specific energy upwards of 200 Whkg^{-1}, but with a maximum specific power being below 350 Wkg^{-1}. By contrast most electrochemical capacitors possess specific power values as high as 10 kW kg^{-1}, but with specific energies in the 5 Wh kg^{-1} range. Yet a key target for an advanced electrical energy storage device is to deliver both high energy and high power in a single system.[35,36]

A hybrid ion capacitor is a relatively new device that is intermediate in energy and powder between batteries and supercapacitors. Since there is the potential to span the energy-power divide between the two systems, hybrid devices are attracting increasing scientific attention.[37,38,39,40,41,42,43,44,45,46,47,48] The hybrid ion capacitor couples a high capacity bulk intercalation based battery-style negative electrode (anode) and a high rate surface adsorption based capacitor-style positive electrode (cathode). When employing Na$^+$ and counter ions such as ClO_4^- as charge carriers, the device is termed NIC, *i.e.* sodium ion capacitor.[38,43,45]

Overall, the NIC field is quite young, with more research into improved electrode materials being desirable. Previously, researchers have primarily focused on improving the power capability of the anode in order to catch up with the fast kinetics of the capacitive cathode.[39,42,44,46] NIC devices have been recently fabricated using the following anode-cathode combinations: V_2O_5/CNT//AC,[38] $Na_xH_{2-x}Ti_3O_7$//AC [43], with AC meaning conventional activated carbon. This creates a necessity to include excess mass (*i.e.* volume), generally several times more than that of the anode, in order to achieve the charge balance between the two electrodes.[39,43,44] The Na ion insertion processes into the bulk of the negative electrodes are known to be substantially more kinetically sluggish than those for Li,[4,49,50] posing a secondary major challenge to achieving attractive Na ion - based hybrid devices.

An inexpensive carbon-based negative electrode with a Na redox potential near Na/Na^+ would not only provide a cost advantage over the inherently more costly inorganic materials but would also maximize the device energy density.[11,40,49,51,52] Ideally such electrode materials would also be truly green,[7,8,20,26,30,31,33,47,53,54,55,56,57,58,59,60,61] being derived from organic waste products that otherwise possess no economic value. Peanuts are a globally cultivated legume food staple, with the peanut shells having only limited commercial end-use as filler in animal feed or as charcoal.[62] In 2010 the peanut plant was cultivated on 21 million hectares worldwide,[63] producing approximately 20 million tons, with an estimated value of 9 billion USD.[64] This produces roughly 6 million tons of peanut shell waste. Researchers have prepared activated carbons from peanut shells and explored their applications in environmental science (*e.g.* sorbents for organic and metal pollutants removal[65,66]) and energy storage (*e.g.* supercapacitor,[67,68] lithium ion battery[69,70]). These "classical" activated carbons were prepared by direct pyrolysis followed by high temperature activation.[62,67,71,72] In terms of the synthesis methodology and by the resultant structure and performance, such ACs are analogous to commercial products, which are micro-scale particulates with tortuous 3D pore networks. In terms of the synthesis methodology and by the resultant structure and performance, such ACs are analogous to commercial products, which are micro-scale particulates with tortuous 3D pore networks. In this work we take an alternative approach: We tailor the synthesis process to take full advantage of the unique structure of the peanut shell and actually achieve two fundamentally different (anode *vs*. cathode) very high performance electrodes from the same precursor.

Results and Discussion

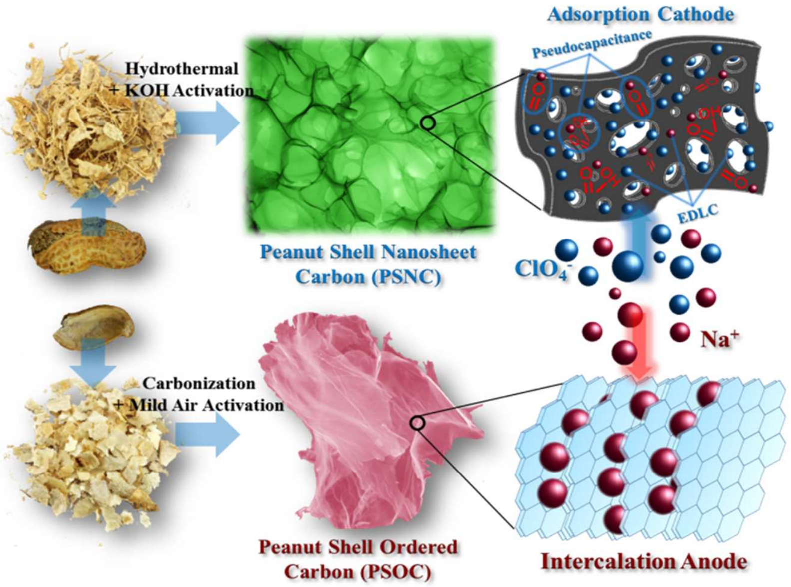

Scheme 1 Material synthesis process employed for each of the electrodes and the relevant cathode/anode charge storage mechanisms in the sodium ion capacitor (NIC).

Scheme 1 illustrates the material synthesis process employed for each of the electrodes, as well as the relevant cathode/anode charge storage mechanisms, to be discussed later in the text. The peanut shell was firstly separated into two parts. The inner portion of the shell was used as the precursor for the negative electrode (designated "anode"). The anodes were prepared by carbonization (1200°C) in argon, followed by a mild low temperature (300°C) activation treatment in air. Unlike conventional high temperature activation, typically performed in excess of 600°C, this treatment was unique in introducing sufficient porosity but not destroying the macroscopic sheet-like architecture of the precursor. Because of their resultant structure, these materials are labelled Peanut Shell Ordered Carbon PSOC. Since not all specimens were activated, we added the ending "-A" *i.e.* PSOC-A to the ones that were. The outer rough shell was employed as the precursor for the positive electrodes ("cathode"). These carbons were prepared by hydrothermal treatment (described in experimental) followed by KOH chemical activation at 800 - 850 °C in argon. Because of their resultant structure, these carbons are labelled Peanut Shell Nanosheet Carbon PSNC. The specific nomenclature is PSNC-*x*-*y*, where *x* refer to the mass ratio between the KOH and the biochar obtained after the hydrothermal treatment, while *y* refer to the activation temperature. A high surface area Commercial Activated Carbon (NORIT A SUPRA, steam activated), labeled CAC, was also employed as baseline for cathode testing.

The decision to employ the inner shell as the anode and the outer shell as the cathode was based on our understanding of the differences in their plant structure, and how those may be transformed to the target final electrodes' microstructure. The peanut shell is primarily a combination of cellulose, hemicellulose and lignin. However its tissue is highly heterogeneous, with the inner versus the outer shell containing different relative fractions and distribution of each phase. Our sodium ion capacitor (NIC) device consists of an intercalation anode and an adsorption cathode, requiring carbons with fundamentally different degrees of graphene ordering, surface area/porosity, and surface functionality for each electrode.

We chose the inner shell for the anode because it is the most homogenous portion of the shell, being primarily composed of lignin. Lignin is a three-dimensional, highly cross-linked polyphenolic polymer without any ordered repeating units. This lignin-rich tissue prevented large-scale formation of equilibrium graphite during high temperature pyrolysis but allowed for pseudographitic ordering of the defective graphene planes. Such ordering results in a structure composed of highly inter-dilated graphene layers (as compared to equilibrium graphite), which is thus able to easily intercalate the large Na ions. The NIC's battery-like ion intercalation anode does not need to possess a high surface area, as ion adsorption was not a significant charge storage mechanism. Therefore the inner shell's relatively homogeneity was not a major concern, as it did not require to be separated into nanosheets, etc. through preferential chemical etching.

Conversely the NICs capacitor-like adsorption cathode required a very high surface area and facile ion diffusion/access through the electrolyte. We were looking for a precursor that ideally could be transformed in to an electrochemically graphene-like analogue. From our previous work on processing plant-based materials we knew that the key to achieving such properties is to begin with a precursor that is highly heterogeneous but with nano-scale periodicity. We needed something where one or several of the phases could be preferentially etched while leaving behind intact sheets or other 2-D structures. The outer skin of the peanut shell was cellulose-rich but highly heterogeneous. It consists of an interconnected cellulosic fibril network (crystalline cellulose), with the individual microfibrils being roughly 10 - 30 nm in diameter. These microfibrils are interlinked by a minority phase of much shorter branched polysaccharide tethers (hemicellulose) and polyphenolic polymers (lignin).[73] Such multi-phase tissue, abundant in cellulose fibrils, is an ideal precursor to achieve interconnected carbon nanosheets through a hydrothermal + chemical activation process, which in parallel adds capacitance enhancing surface functional groups.

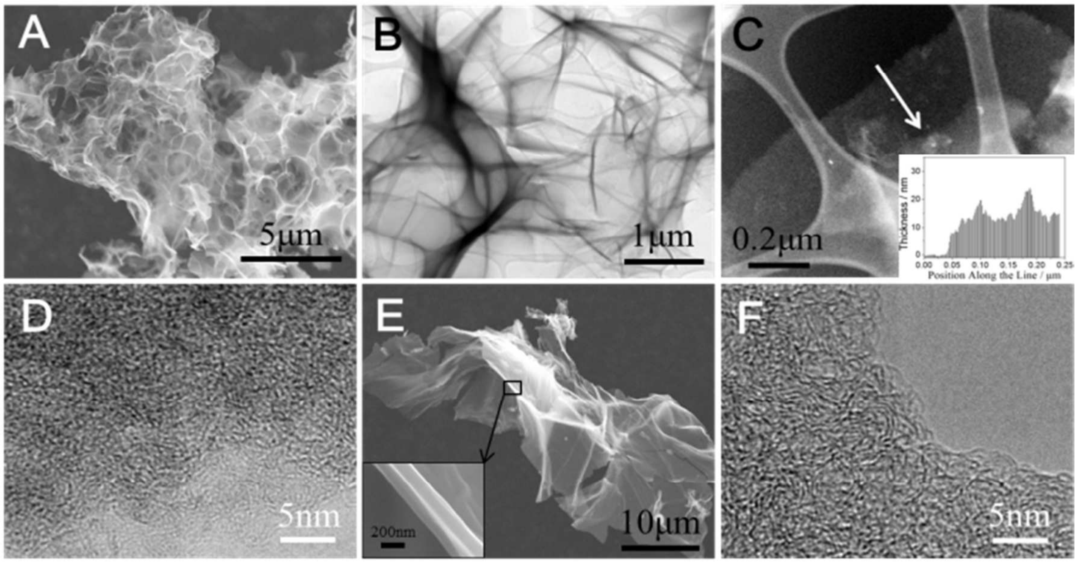

Fig.1 (A) Low magnification SEM micrograph illustrating the macroscopic morphology of PSNC-3-800. (B) TEM micrograph of PSNC-3-800 highlighting the morphology of the carbon nanosheets. (C) HAADF image (holey carbon support also visible) and insert of a thickness profile of PSNC-3-800, measured with low loss EELS along the white arrow. (D) HRTEM micrograph of PSNC-3-800. (E) Low magnification SEM micrograph highlighting the morphology of PSOC-A with an insert highlighting the thickness of the carbon sheet. (F) HRTEM micrograph of PSOC-A.

Figure 1A displays a low magnification scanning electron microscopy (SEM) micrograph of PSNC-3-800. Figure S1D shows CAC, which is a micron - scale 3D particulate. Conversely, PSNC-3-800 morphologically resembles a macroscopically open sponge. Supplementary Figures S1A and B display the SEM micrographs of PSNC-3-850 and PSNC-2-800. Both carbons possess an analogous morphology as PSNC-3-800, although with decreasing levels of macroscopic "openness" in the same order.

The morphology of PSNC is attributable to a synthesis strategy that is tailored to take the maximum advantage of the structure of the outer peanut shell. Under the relatively aggressive conditions of a hydrothermal treatment, the minority non-crystalline components are hydrolyzed and dissolved. However the interconnected cellulosic fibril network is not fully dissolved. Rather, the hydrothermal process degrades the overall crystallinity and loosens the connections between the microfibrils. The hydrothermal process also partially carbonizes them, resulting in the preservation of a cellulose "scaffold" on the micron-scale, as observed in the SEM images. During chemical activation the pores left over from the dissolution of non-crystalline components serve as channels for the capillarity-driven infiltration of liquid KOH, further loosening the microfibril networks to create the carbon nanosheets and punching secondary micro and meso porosity into the structures. A similar phenomenology was employed to explain the formation of sheet like carbon layers from other multi-phase composites containing cellulose fibrils precursors, *e.g.* hemp fiber.[74] In order to reinforce the discussion concerning the rationale for precursor selection, we employed the entire peanut shell as a single precursor, with the same synthesis procedures as PSNC-3-800. Figure S2A shows SEM micrograph of the resultant carbon specimen. The carbon particle did not display the essential macroscopically open sheet-like morphology.

During electrochemical testing the open architecture of PSNC will allow full access of the electrolyte to the active surfaces, minimizing high rate diffusional losses through the liquid. By contrast, commercial activated carbons including CAC are known to contain a tortuous pore network that penetrates microns deep into the particulates. Especially at high scan rates / current densities this will result in significant ion diffusional losses.

Figure 1B shows a transmission electron microscopy (TEM) micrograph of PSNC-3-800, further illustrating the structure of the carbon, which consists of three-dimensional arrays carbon nanosheets. Figures 1C and S3 (A-B) show high angle annual dark field (HAADF) scanning TEM (STEM) micrographs and low-loss electron energy loss spectroscopy (EELS) thickness profiles of the PSNC specimens. PSNC-3-800 has carbon nanosheet thickness in the range of 15 - 25nm, which is thinner than that of PSNC-3-850 (40 - 60nm). Due to the insufficient chemical etching, PSNC-2-800 has the largest carbon sheet thicknesses, being up to 140 nm. Figure 1D presents a high resolution TEM (HRTEM) micrograph of PSNC-3-800, demonstrating the low degree of ordering in the material. The other PSNC specimens were similarly disordered, being shown in Figures S3C and S3D.

The morphology of the PSOC-A and PSOC, which are synthesized from the inner peanut shell, is shown in Figures 1E and S1C. These materials also exhibit a macroscopically open structure, which is unaffected by activation. The insert in Figure 1E highlights the typical sheet thickness, which is on the order of 300 nm. As shown in Figure S2B, the specimen derived from the integral peanut shell is mainly solid µm-size irregular-shaped carbon particles lacking macroscopic openness. The tissue of the inner peanut shell possesses a much higher content of three-dimensional highly cross-linked lignin. During high temperature pyrolysis such a precursor will act as a "hard" carbon, preventing large-scale formation of equilibrium graphite at temperatures high as 1400°C.[49] However during carbonization the material will order locally, creating pseudo-graphitic arrays with dilated intergraphene spacing. As the HRTEM images in Figures 1F and S4 illustrate, PSOC and PSOC-A primarily consist of partially ordered graphene domains, which may be described as "pseudographitic".

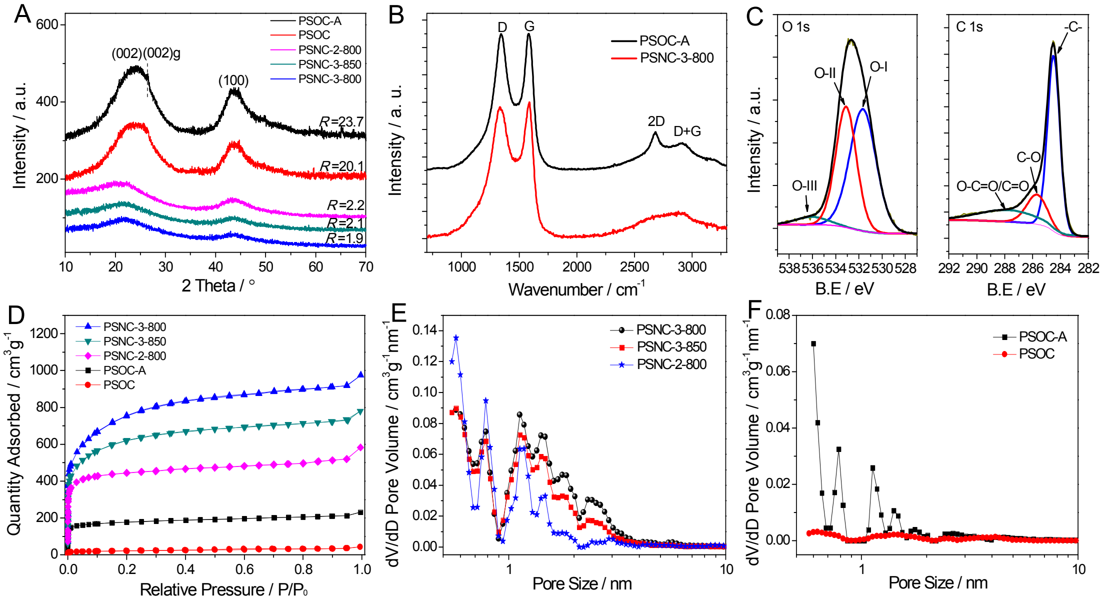

Fig. 2 (A) XRD patterns of the PSNC and PSOC specimens. (B) Raman spectra of PSNC-3-800 and PSOC-A. (C) O 1s and C 1s core level XPS spectra fits for PSNC-3-800. (D) Nitrogen adsorption-desorption isotherms of PSNC and PSOC. (E) Pore size distribution of PSNCs. (F) Pore size distribution of PSOCs, calculated from the adsorption isotherms using DFT method.

Figure 2A shows the X-ray diffraction (XRD) patterns of the PSOC and PSNC. The patterns of PSOC show two broad diffraction peaks that are indexed as (002) and

(100) of the pseudographitic domains. These peaks are barely discernable in PSNC, indicative of its much lower ordering. Moreover the PSOC patterns display the presence of a minor amount (estimated to be ~ 1 wt%) of equilibrium graphite, which is indexed separately. The average graphene interlayer spacing can be calculated from the center position of (002) peaks. As Table 1 shows, the mean integraphene layer spacing (d_{002}) for PSOC is significantly larger than that of graphite (0.3354 nm). We will demonstrate that this dilated intergraphene spacing allows for facile Na ion intercalation into the bulk of the PSOC-based negative electrode. To further understand the graphene plane arrangement in our materials, we employ an empirical parameter (R), defined as the ratio of height of the (002) Bragg peak to the surrounding background.[75] A schematic depicting how R was calculated is shown in Figure S5. It has been argued that the value of R could credibly characterize the concentration of the graphene sheets arranged as single layer, with a larger R indicating a lower percentage of single graphene sheets within a carbon.[75] The R values for PSOC are an order of magnitude higher than they are for PSNC (20-23 *vs.* ~ 2), agreeing with our interpretation of the HRTEM images. Activation of PSOC does increase R from 20.1 to 23.7, presumably by preferentially volatilizing to CO_2 the less ordered portions of the material. The average dimensions of the ordered graphene domains (L_a, L_c) could be calculated by the well-known Scherrer equation, using the full width at half maximum values of (002) and (100) peaks, respectively. As shown in Table 1, the domain thickness is relatively invariant from sample to sample (including for CAC), ranging from 1.51 - 1.84 nm. However with domain

width is twice as large for PSOC *versus* PSNC or CAC (~ 8 nm *vs.* ~ 4 nm).

The structure of the carbons was further investigated by Raman spectroscopy. As shown in Figure 2B and Figure S6, all the specimens exhibit broad disorder-induced D-bands (≈ 1340 cm^{-1}) and in-plane vibration G-bands (≈ 1580 cm^{-1}). The values of the integral intensity of D- and G- bands could be obtained by fitting the spectra (Figure S6), with I_G/I_D being employed to index the degree of graphitic ordering. As Table 1 shows, for PSOC the I_G/I_D values are 1.01 - 1.1, for PSNC they are 0.41 - 0.62, while for CAC the ratio is 0.26. PSOC also exhibited second order 2D and D+G peaks, which are also associated with their more ordered structure.[76] PSNC displayed an electrical conductivity in the range of 181 - 227 S cm^{-1}, being a factor of five higher than that of CAC (43 S cm^{-1}). Although we were unable to press PSOC into sufficiently dense "pucks" as to perform satisfactory 4 point probe conductivity measurements, it is expected that these highly ordered - low surface area carbons will be similarly much more conductive than CAC.

Table 1 Carbon structure, electrical conductivity and textural properties of Peanut Shell Nanosheet Carbon (PSNC) and Peanut Shell Ordered Carbon (PSOC), with baseline commercial activated carbon CAC also shown.

Sample	Carbon Structure					s (S cm^{-1})	Textural Properties			
	d_{002} (Å)	R	L_a (nm)	L_c (nm)	I_G/I_D [a]		S_{BET} (m^2 g^{-1})[b]	V_t (cm^{3}g^{-1})[c]	micropores %	mesopores %
PSNC-3-850	4.12	2.1	4.43	1.51	0.56	227	1998	1.21	70.2	29.8
PSNC-3-800	4.13	1.9	3.75	1.71	0.41	181	2396	1.31	64.5	35.4
PSNC-2-800	4.11	2.2	4.49	1.55	0.62	192	1376	0.91	77.5	22.5
PSOC	3.78	20.1	7.95	1.80	1.10	-	78	0.074	45	55
PSOC-A	3.79	23.7	8.04	1.84	1.01	-	476	0.31	77.8	22.2
CAC	3.72	3.8	4.20	1.84	0.26	43	2050	1.17	67.7	32.3

[a] I_D and I_G are the integrated intensities of D- and G- band. [b] Surface area was calculated with Brunauer-Emmett-Teller (BET) method. [c] The total pore volume was determined at a relative pressure of 0.98.

Figure 2D shows the nitrogen adsorption-desorption isotherms of PSNC and PSOC, while Figure 2E-F shows their pore size distributions (obtained by density functional theory (DFT)). The same analysis for the CAC baseline is shown in Figure S7. Table 1 provides the porosity characteristics of the peanut shell derived materials and of CAC. Type I/IV isotherms could be found for all the PSNC specimens, which all possess considerable porosity and high surface areas. The surface area and the pore volume fraction of micropores *vs*. of mesopores (and total pore volume) depend on the activation conditions. Overall both the highest surface area (2396 m^2 g^{-1}, being desirable for maximizing the total ion adsorption) and the highest fraction of mesopores (35.4%, being desirable for rapid electrolyte diffusion) were achieved in the PSNC-3-800. A higher activation temperature or a lower ratio of KOH to carbon resulted in a reduction of both attributes. CAC actually possesses an on par surface area (2050 m^2 g^{-1}) and mesopore content (32.3%). However due to its lower electrical conductivity and a "closed" particulate morphology CAC will be demonstrated to be a far inferior electrode at high charge rates.

X-ray photoelectron spectroscopy (XPS) and combustion elemental analysis were employed to investigate the surface and bulk chemical composition of PSNC and PSOC. Figure S8 displays the XPS survey and fitted high-resolution spectra. Table 2 lists the surface composition of the carbons, the oxygen functionalities, and the bulk C, O, N and H results of the elemental analysis. Based on the XPS survey spectra, the content of impurities (Si, Cl) is 0.9 wt% in total. Other potential impurities that may be present in plant-based precursors (*e.g.* P, K, Mg, Ca) were below the detection limits of XPS analysis, being both volatilized during synthesis and further removed by the post-synthesis HCl wash.

Table 2 Surface chemistry of PSNC and PSOC, with baseline CAC also shown.

Sample	Surface Chemistry (XPS)			Functionality (% of total O 1s)			Elemental analysis[a]			
	C (wt%)	N (wt%)	O (wt%)	O-I	O-II	O-III	C (wt%)	N (wt%)	O (wt%)	H (wt%)
PSNC-3-850	89.45	0.85	9.70	44.15	51.87	3.98	90.44	0.93	7.41	0.21
PSNC-3-800	85.91	0.58	13.51	53.94	41.83	4.23	86.51	0.65	12.21	0.13
PSNC-2-800	87.31	0.96	11.73	44.58	43.04	12.38	88.31	0.94	9.97	0.33
PSOC	93.70	0.73	5.57	55.72	29.44	14.83	92.82	0.46	5.04	1.08
PSOC-A	92.94	0.97	6.09	39.41	55.28	5.31	91.85	0.74	5.71	1.10
CAC	95.35	~0	4.65	45.32	47.15	7.53	94.12	0.12	4.34	0.43

[a] Weight percent of elements obtained from combustion analysis.

The unactivated biochar obtained after the hydrothermal process possessed a significant content of O (34.2wt%, results not shown). After chemical activation, a large portion of oxygen heteroatoms is preserved, with 11.7wt%, 13.5wt% and 9.7wt% oxygen content for PSNC-2-800, PSNC-3-800 and PSNC-3-850 respectively. The high-resolution O 1s and C 1s XPS spectra of PSNC-3-800 is shown in Figure 2C, with the same data for the other materials being displayed in Figures S8 B-F. The high resolution O 1s spectra could be deconvoluted using 3 peaks representing the 3 different types of oxygen functional groups: C=O quinone type groups (O-I, 531 eV), C-OH phenol/C-O-C ether groups (O-II, 532.4 eV), and COOH carboxylic groups (O-III, 535.4 eV). The surfaces in all the specimens are primarily covered by O-I and O-II functionalities, with O-III being a relative minority. For instance in PSNC-3-800 the relative weight percent is 53.9% for O-I, 41.8% for O-II and 4.2% for O-III. In PSOC and PSOC-A the amount of O was much lower, being 5.6wt% and 6.1wt%. In all PSNC and PSOC the N content was below 1wt%. Baseline CAC contained 4.65wt% O and negligible N. The N content in all carbons is sufficiently low that it is not expected to meaningfully contribute to the charge storage capacity.

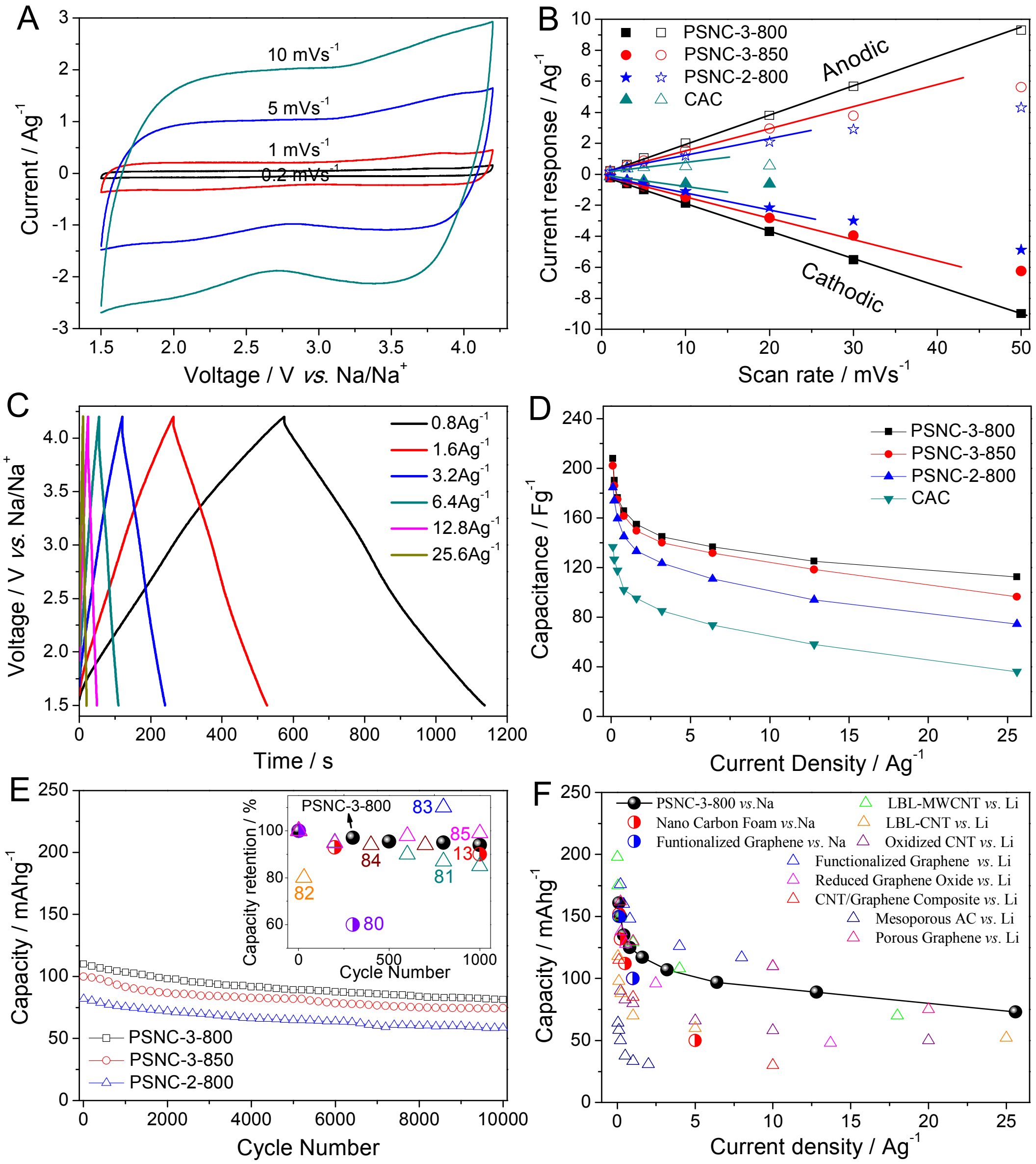

Fig. 3 Half – cell performance of PSNC and CAC, tested between 1.5 - 4.2 V *vs.* Na metal. (A) Cyclic voltammograms (CVs) of PSNC-3-800. (B) Dependence of anodic and cathodic current (at 2.75 V) on scan rate, indicating the deviation from linear behavior. (C) Galvanostatic discharge/charge profiles of PSNC-3-800, at current densities from 0.8 to 25.6 Ag^{-1}. (D) Specific capacitance of PSNC versus current density. (E) Cycling stability of PSNC (tested at 3.2 Ag^{-1} for 10,000 cycles), with an insert comparison to state-of-the-art Na and Li cathodes in hybrid devices. (F) Specific capacity *vs.* current density for PSNC-3-800, comparing with best literature reports for both Na (tested at same voltage window) and Li (tested at the wider 1.5-4.5 V *vs.* Li/Li$^+$) hybrid cathodes.

Figure 3 shows the electrochemical performance results for PSNC, which will be employed as the cathode in the hybrid NIC device. Here PSNC was tested in a half-cell configuration *versus* Na metal, in a voltage window previously employed for hybrid Na-based cathodes (1.5 - 4.2V). This range maximized the operating voltage window without decomposing the electrolyte, or intercalating ions into the bulk of the carbons to an appreciable extent.[49, 77, 78] Upon positive polarization the PSNC electrode will reversibly adsorb ClO_4^- and reversibly release Na^+. Capacitance is achieved both by EDLC of ClO_4^-, and through a pseudocapacitive interaction of Na^+ with surface defects and oxygen functionalities.

As shown in Figure 3A, the CV curves of PSNC-3-800 electrode display a box-like shape, indicative of typical EDLC behavior, overlaid with pseudocapacitive humps. Figure S9 shows the same CV data for PSNC-3-850, PSNC-2-800 and CAC carbons. The level of *IR* loss - induced distortion in the CVs at higher scan rates for the materials goes effectively in the order of the "openness" of the structures: With increasing scan rate (0.2 - 10 mVs^{-1}) the PSNC-3-800 specimen displayed negligible shape distortion. PSNC-3-850 was the second least distorted, the PSNC-2-800 was the third least distorted. Of all the carbons, the high scan rate CVs of the particulate-like CAC were by far the most distorted.

Figure 3B displays the current dependence on the CV scan rate, measured at 2.75 V. At scan rates from 1 to 50 mV s^{-1} the PSNC-3-800 electrode maintained linearity. For PSNC-3-850 and PSNC-2-800, the onset for deviation from linearity is 25 mV s^{-1}

and 15 mV s^{-1}, respectively. For CAC, the charge storage reaction became diffusion limited at very low rates, *i.e.* below 5 mV s^{-1}. A transition from a linear dependence of current to square root dependence is considered an indicator of the onset of diffusion-limited reactions,[79] and supports the argument that the ion transfer kinetics for the open PSNC structures is much more facile as compared to CAC. Since the charge storage mechanisms for PSNC are surface adsorption based, one can argue that the carbons' open structure reduces the ion diffusional limitations in the electrolyte (rather than in the bulk). Differences in pore shapes may also play an important role. Pores in PSNC could provide smoother inner-pore transport channels for ions as compared to conventional activated carbons, reducing the "traffic jam" effect discussed in ref. [30,74]

Figures 3C and S10 show the galvanostatic charge/discharge profiles for PSNC as well as for CAC. For the PSNC electrodes the curves are symmetrical with low *IR* drops. Conversely, CAC is quite distorted at higher current densities (Fig. S10D). Figure S11 displays the measured *IR* drop of each carbon at various current densities. As indicated, CAC's pore tortuosity and inferior electrical conductivity both contribute to the larger CV distortion at high rates and the higher *IR* drops.

Figure 3D shows the specific capacitance of the PSNC and the CAC electrodes as a function of current density. The optimized PSNC-3-800 delivered a capacitance of 213Fg^{-1} at current density of 0.1Ag^{-1}, which gave surface normalized capacitance of

8.9 μFcm^{-2} (based on BET surface area). The PSNC electrodes consistently outperform CAC through the entire current range of testing. However the performance difference is most stark at the very high currents, where electrolyte diffusional limitations the manifest: At 25.6 Ag^{-1} PSNC-3-800 delivers 119 Fg^{-1} while CAC delivers 36 F/g. Figure S12A shows the electrochemical data for the cathode carbon derived from the integral peanut shell as the precursor. Its inferior capacitance further proves the essential function of the macroscopic openness and the sheet-like morphology of PSNC-3-800.

Overall the PSNC-3-800 electrode offers the best performance, which may be attributed to its optimum combination of O content, surface area and mesopore content, the later becoming critical at high scan rates. The most reactive oxygen functional groups should be the quinone type groups (C=O/O-C=O, O-I type) due to the unsaturated carbon-oxygen double bond. As covered earlier, all PSNC materials possess significant O-I content, with PSNC-3-800 being the richest both in terms of weight fraction (53.94%) and the total amount. It has been previously argued that between 1.5-4.2V *vs*. Na/Na^{+} there is substantial charge storage capacity associated with reversible Na^{+} binding to this moiety.[13,80] This therefore is another reason for the optimum performance in PSNC-3-800 *versus* PSNC-3-850 or PSNC-2-800. While CAC contains an analogous fraction of O-I, its overall oxygen content is three times lower.

The cycling performance of PSNC, tested at 3.2 Ag^{-1}, is shown in Figure 3E. The figure also contains an insert that compares our data to state-of-the-art Na and Li cathodes previously employed in hybrid devices and published in scientific literature. For a consistency with the PSOC data, these results are presented in terms of specific capacities ($mAhg^{-1}$) rather than capacitances. The capacitance C (F g^{-1}) is defined as $C = i \times t / V$, where i is the active mass normalized current density and t is discharge time obtained from the galvanostatic discharge curve. The voltage window V is defined as $V = V_{\max} – V_{\min}$, where $V_{\max}$ is the voltage at the beginning of discharge after the IR drop and $V_{\min}$ is the voltage at the end of discharge. The specific capacity Q of a half-cell is $Q = i \times t$. Thus a conversion of a measured capacitance to a measured capacity requires a straightforward multiplication of C by V. For instance a capacitance of 140 F/g with a voltage window of 2.7 V will yield a specific capacity of 105 $mAhg^{-1}$ (*i.e.* 140 × 2.7/3.6).

It is important to point out that the scientific convention for cycling of electrodes in hybrid battery - supercapacitor Li and Na devices remains similar to that for testing of conventional battery materials, rather than to materials employed for EDLC supercapacitors or for faradaic pseudocapacitors (e.g. surface redox oxides such as Co_3O_4). In literature for hybrid Na and Li electrodes, cycling is often completed as early as after 1,000 cycles, with testing being rarely performed beyond 5,000 cycles. The PSNC-3-800, PSNC-3-850 and PSNC-2-800 electrodes retained 94%, 91% and 92% of the initial capacity after the usual 1000 cycle test span employed for qualifying hybrid system cathodes[13,81,82,83,84,85]. Previously published cycling results are overlaid with our data, Na being half full circles and Li being open triangles. PSNC cycling performance is among the state-of-the-art for both Li[81,82,83,84,85] and Na[13,80] systems, which is notable since researchers empirically observe Na electrodes cycling worse than Li electrodes. The PSNC cathodes kept working well throughout the 10,000 cycles tested. At the 5,000th cycle, PSNC-3-800, PSNC-3-850 and PSNC-2-800 retained 82%, 84% and 81% of the initial capacity. After 10,000 cycles these values were 73%, 74%, 73%. We attribute the cycling loss to a gradual degradation of the surface oxygen moieties rather than to bulk changes of the carbons' structure. By contrast the CAC electrode retained only 61% of its initial capacity after 5,000 cycles.

Figure 3F displays the current density dependence of the capacity in PSNC-3-800 and compares it to various advanced carbon-based materials previously employed as cathodes in both Na and Li hybrid devices. The PSNC-3-800 electrode (black circles) is quite attractive in comparison to published Na-based systems (half full circles) tested at an identical voltage window[13,80]. In fact it actually performs on par with some of the best cathodes for hybrid Li devices (open triangles), which are normally expected to display higher capacities and rate capabilities than Na. The fact that our Na adsorption cathode is competitive with Li adsorption cathodes is highly notable since Na is a 39% larger ion that is much more prone to electrolyte solution diffusional limitations while inside the pores of the carbon (a key rate limiting step for ion adsorption electrodes). The Li cathodes are also tested with a wider voltage window (1.5-4.5 V), further giving them a "leg up" over Na in terms of the measured capacity. The Li electrodes include mesoporous AC's, [86] functionalized graphene,[82,83,87] CNT/graphene composite,[88] and functionalized CNTs[81,85,89].

We also prepared PSNC-3-800 electrode with a mass loading of 2 mg cm^{-2} and tested it identically. As shown in Figure S13A, although the mass loading is 5 times higher, the capacities were at maximum 17% lower. To estimate the density of an electrode which would operate in a commercial device, we prepared a 15 mg cm^{-2} mass loading electrode in a pressed state (100 MPa). As shown in Figure S14A, the PSNC-3-800 electrode was approximately 240 μm thick, giving a packing density of 0.62 g cm^{-3}. This is on par with the 210 μm, 0.71 g cm^{-3} of an identically mass loaded and pressed CAC electrode. We calculated the volumetric capacity of the PSNC-3-800 electrode based on the above density value, with the results being shown in Figure S15A.

Figure 4 shows the electrochemical performance results for PSOC, which will be employed as the anode in the hybrid device. Here PSOC was tested in a half-cell configuration *versus* Na metal. Figures 4A and S16A display the CV curves of PSOC-A and PSOC half-cells, tested between 0.001 and 3V. The CV's display a pair of sharp cathodic (centered at 0.016 V) and anodic peaks (centered at 0.11 V), indicating minimum hysteresis between the charge and the discharge process. Figure

4B shows the galvanostatic data for PSOC-A tested at a current density of 0.1 A g^{-1} (~ 1/3C), at cycles 1, 2, 5 and 10. The same charts for PSOC and the galvanostatic curves as a function of current density (at 5th cycle at each current density) are shown in Figure S16B. As shown in Figure 4B, galvanostatic curves possess relatively flat charge - discharge profiles, with the majority of the capacity (discharge: 181 of 315 $mAhg^{-1}$) being accumulated below 0.1 V. The flat charge - discharge plateau and the low voltage are desirable for maximizing both the energy density and the voltage profiles of full devices.

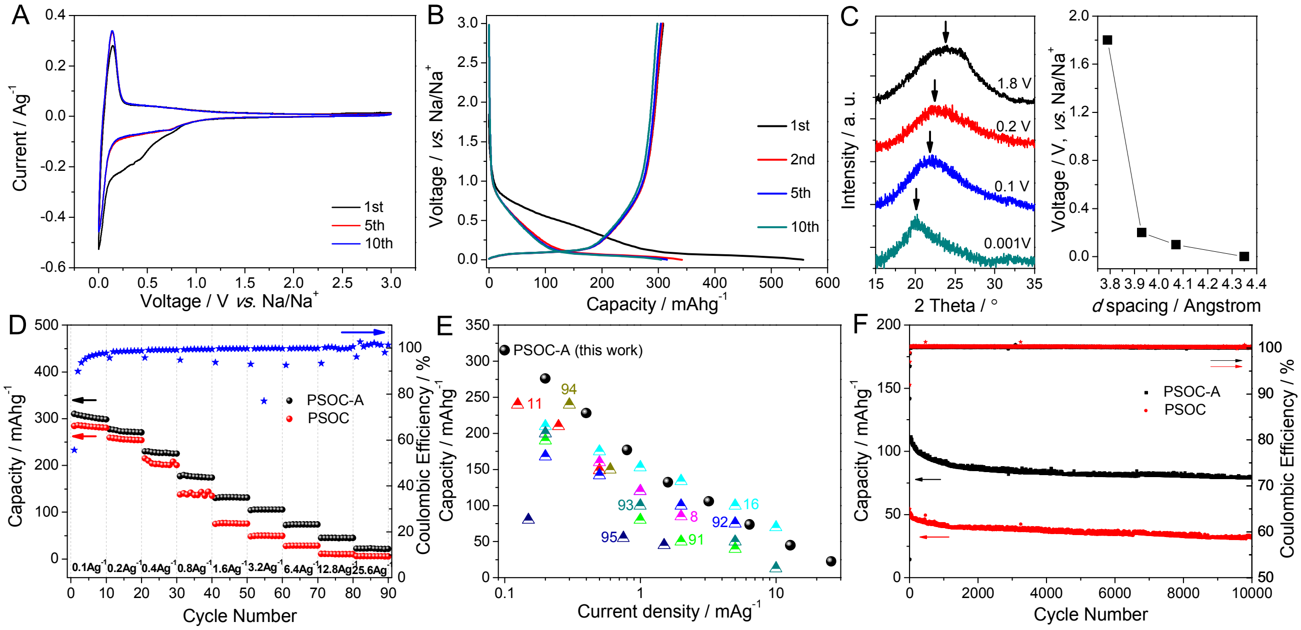

Fig. 4 Half - cell performance of PSOC and PSOC-A. (A) CVs of PSOC-A, tested at 0.1 mVs^{-1}. (B) Galvanostatic discharge/charge profiles of PSOC-A, tested at 0.1Ag^{-1}. (C) (left) XRD spectra for PSOC discharged at 50 $mAhg^{-1}$ to 0.2, 0.1 and 0.001 V. (right) The mean interlayer spacing at several cut-off voltages. (D) Rate performance and CE of PSOC and PSOC-A. (E) Rate capability comparison of PSOC-A with the literature published carbonaceous materials employed as Na anodes. (F) Cycling capacity retention and CE of PSOC and PSOC-A, tested at 3.2 Ag^{-1} for 10,000 cycles.

Figure 4C displays the *ex-situ* XRD patterns of PSOC electrodes discharged to different cut-off voltages (1.8, 0.2, 0.1 and 0.001 V *vs*. Na/Na$^+$) at a current density of 50 mAg^{-1}. The sodiated carbons were kept in an argon container up to the point of XRD testing. The raw XRD plots along with the insert of the calculated mean *d*-spacing demonstrate sodiation-induced dilation of the intergraphene layers that is synonymous with ion intercalation. This is fundamentally different low voltage charge storage behavior as compared to nanoporous carbons tested against Li metal, where metal plating was indeed experimentally proven to be a key contributor to the total capacity.[90]

We employed air activation to introduce limited additional porosity into the PSOC electrodes. This would both improve the electrolyte access to the bulk of the material and reduced the solid-state diffusion distances due to a lower effective sheet thickness. As shown in Figure S16E, through the entire scan rate range of interest, both the unactivated and the activated electrodes display nearly a square root dependence of the peak current on scan rate. This indicates that the charge storage process for both PSOC and PSOC-A is diffusion-limited, which is expected for intercalation. However as shown in Figure 4D, PSOC-A exhibited much improved rate capability. At low currents the capacities are not that dissimilar, for example being 315 *vs*. 290 mAhg^{-1} at 0.1 Ag^{-1}. At higher currents, such as 3.2 Ag^{-1} (~ 10C), activation makes a tremendous difference; effectively doubling the capacity from 51 to 107 mAh/g. According to Figure 4E the rate performance of PSOC-A is among the most favorable in comparison to various carbonaceous materials previously tested as anodes in Na half-cells.[8,11,91,92,93,94,95]

As shown in Figure S13B, at the 2 mg cm^{-2} mass loading the current density dependence of specific capacity of PSOC is only slightly lower relative to the 0.4 mg cm^{-2} loading values. Tested within the current density range 0.1 to 25.6 Ag^{-1}, the capacity of the 2 mg cm^{-2} electrode is at most lower by 15%. Figure S14 shows that in a pressed state the 15 mg cm^{-2} PSOC-A electrode is 100 µm thick with a packing density of 1.5 g cm^{-3}, while electrodes identically synthesized from commercial LIB-electrode grade graphite are 80 µm and 1.87 g cm^{-3}. Figure S15B displays the volumetric capacity of PSOC-A electrode at various currents, the calculation being based on an electrode packing density of 1.5 g cm^{-3}.

According to Figure 4F the cycled PSOC-A electrode retained 75% of its original capacity after 10,000 cycles, with coulombic efficiency being at 100% (within the resolution of the instrument) after the first 5 cycles. Such results are highly unusual even for Li anode systems (apart from commercial graphite), since electrode decrepitation and concomitant loss of electrical contact with the current collector inevitably occurs due to repeated volume expansion/contraction associated with charging. However such cycling stability is even more unique for anodes that employ Na as charge carriers due to their larger diameter. The favorable cycling performance of PSOC-A compared to previously published materials may be attributed to its unique "pseudographitic" structure that allows for facile intercalation of large amounts of Na at low voltages. The excellent rate capability results from the very short diffusion distances due the carbons' intrinsic sheet-like morphology further boosted by activation-introduced porosity. As shown in Figure S12B, the carbons derived from the integral peanut shells exhibit much worse rate performances. Materials such as CAC, which are much less ordered and less diffusionally accessible, will offer neither the low-voltage flat-capacity plateau nor the rate capability.

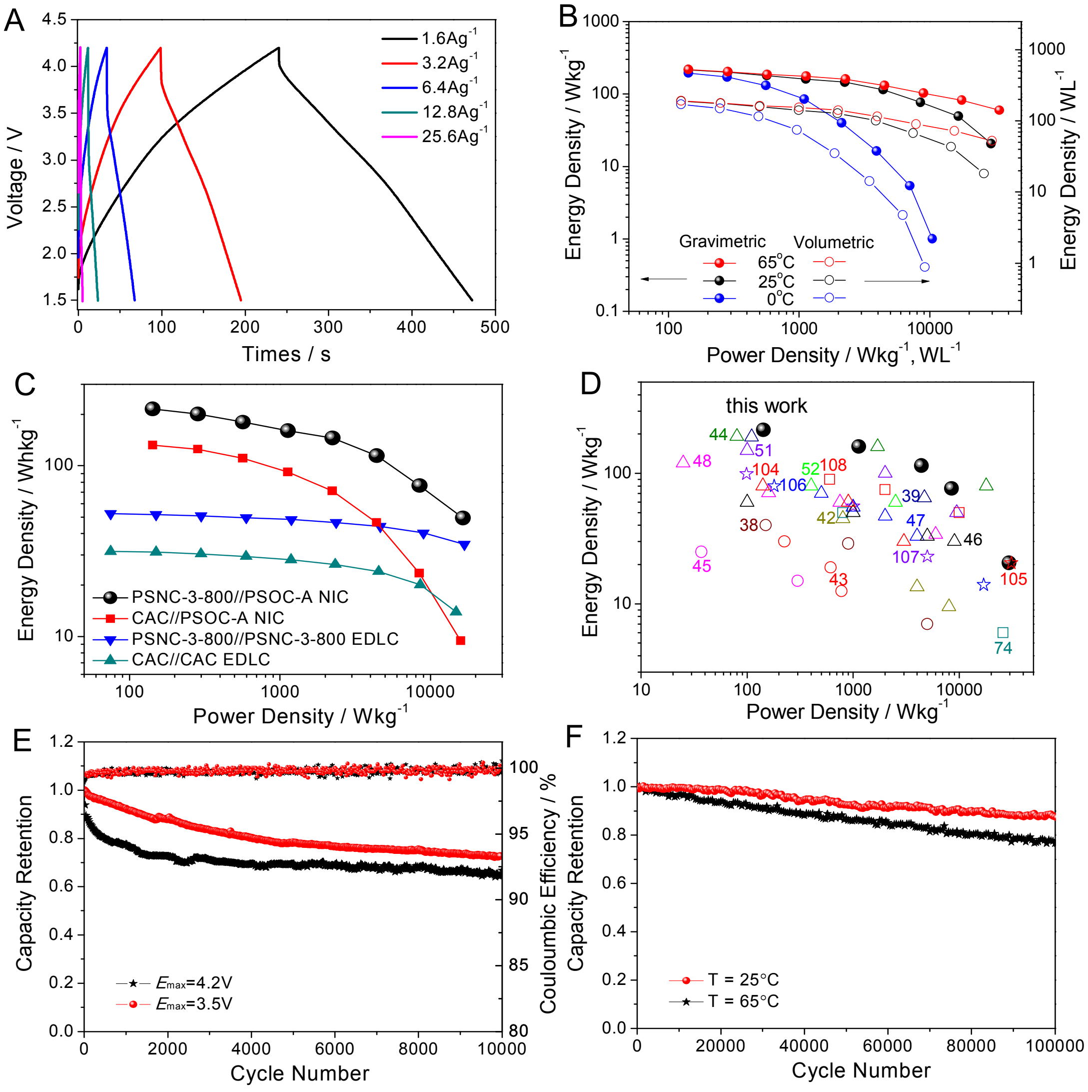

Fig. 5 Electrochemical performance of the hybrid Na-ion capacitors (NICs). (A) Galvanostatic profiles of PSNC-3-800//PSOC-A, the low current density results being shown in Figure S17. (B) Ragone plot of PSNC-3-800//PSOC-A at 0°C, 25°C and 65°C. The calculated energy and power densities are based on the total mass (solid) or volume (hollow) of the active electrodes. (C) Ragone plot (active mass normalized) comparing a device based on PSNC//PSOC to CAC//PSOC and to symmetric PSNC//PSNC and CAC//CAC systems. The PSNC//PSNC and CAC//CAC store charge based on EDLC only. (D) Energy - power density performance comparison (all active mass normalized) of PSNC-3-800//PSOC-A *versus* state-of-the-art reported energy storage systems in literature. (○:Na-ion capacitor, △:Li-ion capacitor, ☆:Aqueous asymmetric EDCL + faradaic capacitor, □: Ionic liquid EDLC capacitor). (E) Cycling stability and coulombic efficiency of PSNC-3-800//PSOC-A, tested at 6.4 Ag^{-1} for 10,000 cycles. (F) PSNC-3-800//PSOC-A devices were tested at 25°C and at 65°C, in both cases undergoing 100,000 cycles at 51.2 Ag^{-1} within a voltage window of 1.5-3.5V.

We combined the two peanut derived carbons to create hybrid sodium ion capacitors (NICs) with an unparalleled performance for Na class of hybrid devices that actually rivals Li ion capacitors (LICs). For the reasons outlined earlier, one normally does not expect NICs to perform as well as LICs in either rate capability or cycling stability. The rationale for employing PSNC as the cathode and PSOC as the anode is as follows: The PSNC is ideally suited as the cathode since it possesses a relatively large charge storage capability and rate performance in the high voltage region, i.e. 1.5 - 4.2V *vs*. Na/Na^+. When employing the PSOC as the anode we can fully utilize the large plateau capacity in the low voltage region, i.e. near and below 0.1 V *vs*. Na/Na^+. We point out that the device would have poor performance if the electrodes were to be swapped. The PSOC anode is a low surface area insertion electrode, with almost all of its capacity being below 0.5 V *vs*. Na/Na^+. It would store negligible charge if employed as cathode swinging through a positive voltage range in a device.

Optimizing device performance consists of achieving the widest possible working voltage window without decomposing the electrolyte, while maximizing the capacity of both electrodes. Both of these targets could be realized when the PSOC anode operates within its plateau region while PSNC cathode swings through the high voltages. In accordance with the principle of balanced charge passing through the cathode and the anode ($Q_{\text{cathode}} = Q_{\text{anode}}$), the electrode mass ratio ($m_{\text{cathode}}/m_{\text{anode}}$) was kept at 1:1. This is based on a capacity of 161 mAhg^{-1} for PSNC-3-800 (discharged at 0.1A g^{-1} to 1.5 V *vs*. Na/Na^{+}) and a 0.1 V *vs*. Na/Na^{+} plateau capacity of 181 mAh g^{-1} for PSOC-A at the same rate. The total voltage window for the NIC was 2.7 V. *It is important to differentiate the total voltage window for the assembled device presented in Figure 5, from the voltage windows for the half-cells vs. Na/Na^{+} presented in Figure 3*. The *device* voltage range was purposely kept at 1.5 - 4.2 V (rather than at 0 - 2.7 V) so as to maintain the cathode operating in the ion surface adsorption regime while limiting ion insertion. Since the capacities of the two electrodes are roughly balanced, upon charging of the device the cathode positively swings by ~ 2.6 V, while the anode negatively swings by ~ 0.1 V (i.e. the flat plateau) to become fully sodiated.

Prior to assembly and testing of the NIC devices, both electrodes were preconditioned in half-cells (i.e. vs. Na/Na^{+}). The PSOC anode was firstly galvanostatically (50 mAg^{-1}) cycled three times between 0.001 - 3 V *vs*. Na/Na^{+}, and then discharged to a cut-off voltage of 0.1 V *vs*. Na/Na$^+$. This left it right above the onset of its high capacity intercalation plateau. The PSNC cathode was discharged (50 mAg^{-1}) to a cut-off voltage of 1.5 V *vs*. Na/Na$^+$, leaving it sodiated to its target capacity. The specific energy and specific power values of assembled NICs were calculated as follows: $E = P \times t$, $P = \Delta V \times i$, $\Delta V = (V_{\max} + V_{\min})/2$, in this case i being the current normalized by the total active mass in both electrodes, $V_{\max}$ is the voltage at the beginning of discharge after the *IR* drop and $V_{\min}$ is the voltage at the end of discharge.

The performance of the NIC device is shown in Figure 5. Results in Figures 5A-E show devices tested at 1.5 - 4.2 V. Figure 5E and 5F also shows devices tested in a narrower voltage window of 1.5 - 3.5 V. Figure S18 shows a device tested in a voltage window of 2.2 - 3.8 V, which is the identical range specified for an advanced hybrid Li ion capacitor that is commercially available.[96]

Figures 5A and S17 provide the galvanostatic charge and discharge profiles of the hybrid NIC devices at intermediate/high and at low current densities, respectively. The profiles display the desirable symmetric characteristics with low *IR* drops. At a current density (normalized by mass of anode) of 3.2, 6.4 and 12.8 A g^{-1}, the discharge capacity normalized by that active mass is 83, 57 and 36 mAh g^{-1}. This equals 41.5, 28.5 and 18 mAh g^{-1} (*i.e.* 60 Fg$^{-1}\times$2.5V/3.6, 44.3 Fg$^{-1}\times$2.32 V/3.6, and 30 Fg$^{-1}\times$2.15 V/3.6) when normalized by the active mass in the device.

Figure S19 shows the Nyquist plots of PSNC-3-800//PSOC-A and CAC//PSOC-A devices. The spectra were fitted by an electric equivalent circuit model shown in Figure S20. The lower equivalent series resistance (R_{es}) for PSNC-3-800//PSOC-A (7.47 Ω) *vs.* CAC//PSOC-A (15.85 Ω) is attributed to a combination of superior electrical conductivity and reduced ion diffusion losses. The PSNC-3-800//PSOC-A device also demonstrated a lower charge transfer resistance (R_{ct} =12.01 Ω *vs*. 21.44 Ω), which may also be attributed to a less tortuous pore network.

Figure 5B displays the Ragone plot of PSNC-3-800//PSOC-A NIC at different temperatures, tested at 1.5-4.2V. The gravimetric energy and power density is based on the total active mass in both electrodes. The volumetric energy and power is also plotted, being estimated from a rule of mixtures of the experimentally measured volume of the active cathode and anode. The device worked well at a wide temperature range (*i.e.* 0-65°C), yielding very promising energy and power combinations. At 65°C, a superb gravimetric energy density of 60 Wh kg^{-1} is obtained at a power density as high as 34,000 W kg^{-1}. At the same temperature a volumetric energy density of 52 Wh L^{-1} is achieved at a power density of 30,000 W L^{-1}. A factor of 1/5 could be used to extrapolate the volumetric performance of a device with realistic mass loading from the performance based on the active materials alone.[97,98] This conversion qualitatively (different device size, packaging, etc.) places our button cells in the range of commercial LIC devices.[99] A volumetric (active electrode or device) based comparison with scientific LIC and NIC literature is difficult as energy/power data is presented normalized by mass only.[38,39,43,44,45,47,48,51,52]

Figure 5C displays the Ragone plot of PSNC-3-800//PSOC-A NIC at room temperature, with the specific energy/power density being based on the total mass of the active materials. The figure also shows a NIC based on CAC//PSOC-A, as well as symmetric EDLC devices based on CAC//CAC and PSNC-3-800//PSNC-3-800. Here the voltage window was 1.5 - 4.2 V, except for the symmetric EDLC devices which were tested within a voltage of 0 - 3V, *i.e.* actually a wider window than for the hybrids. However the EDLC systems are markedly inferior to the PSNC-3-800//PSOC-A configuration. In fact, the PSNC-3-800//PSOC-A system is superior at both low and high power, sacrificing nothing to the EDLC configurations, which are supposed to be superior at high rates. This is a direct testament of the exquisite high-rate intercalation kinetics of the PSOC anode, since solid-state diffusion is normally considered the rate-limiting step for Na battery electrodes. Even at the very power of 16,500 Wkg^{-1} the PSNC-3-800//PSOC-A device delivers a respectable 50 Whkg^{-1} of energy.

It is instructive to compare the energy - power characteristics of our device to the state-of-the-art reported in literature. This is shown in Figure 5D. The figure actually plots four types of systems: NICs, LICs, classical asymmetric aqueous electrolyte based supercapacitors, and ionic liquid electrolyte based supercapacitors that store charge by EDLC. A key distinction between NICs/LICs versus asymmetric aqueous electrolyte based supercapacitors (often also termed "hybrids"), is that for the latter electrical charge is primarily stored by a combination of EDLC and surface pseudocapacitance. Unlike for NICs and LICs, there is negligible ion insertion into the bulk of the anode. While pure EDLC systems may cycle for up to 1,000,000 cycles (albeit at a lower energy), optimized asymmetric aqueous electrolyte based supercapacitors typically last 10,000 cycles and may fail by dissolution and/or coarsening of the oxide[100,101,102,103].

The Li/Na ion capacitors listed include various systems coupling a battery anode and a capacitor cathode, such as, AC//graphite (Li^+),[51] AC//hard carbon (Li^+),[52] AC//$Li_4Ti_5O_{12}$ (Li^+),[47,48] AC//TiO_2-RGO (Li^+),[42] 3D-porous graphene-sucrose//$Li_4Ti_5O_{12}$/G (Li^+),[104] AC//3D-TiO_2/CNT (Li^+),[46] 3D-Graphene//Fe_3O_4-graphene (Li^+),[39] AC//V_2O_5-CNT (Na^+),[38] AC//$Na_xH_{2-x}Ti_3O_7$ (Na^+),[43] AC//$NiCo_2O_4$ (Na^+),[45] AC//AC/MnO (Li^+)[44]. The supercapacitors mentioned include asymmetric aqueous systems like activated-graphene//MnO_2/activated-graphene,[105] $Ni(OH)_2$-graphene//porous graphene,[106] graphene//2D-MnO_2,[107] and symmetric liquid ion systems.[74,108] As may be seen form this master comparison plot, the system developed in the current study is overall quite promising.

The cycling stability of the PSNC-3-800//PSOC-A NIC was firstly investigated at a current density of 6.4 Ag^{-1}. As shown in Figure 5E, using a maximum voltage of 4.2 V the device will retain 79% of its initial capacity after 1,000 cycles, 69% after 5,000 cycles, and 66% after 10,000 cycles. When we employed a smaller cut-off voltage of 3.5 V, the capacity retention increases to 81% at cycle 5,000 and 72% at cycle 10,000. We hypothesize that this improvement corresponds to reduced rates of degradation in the PSNC oxygen functionalities at the lower potential window. At both voltage windows the hybrid capacitors displayed excellent coulombic efficiencies, being near 100% during cycling. As a comparison, NIC device reported in previous in literature displayed 27, 22 or 37% capacity decay after a limited number of cycles (~1,000, or 2,000) at lower voltage region (below 3V).[38,43,45] As Table S1 demonstrates, our cyclability is actually comparable to the previously published LIC devices.[39,40,44,47,51,52,109] For reasons ascribed to the higher levels of volume expansion for a comparable capacity associated with Na vs. Li insertion, achieving an on par cyclability with a NIC is indeed a notable feat.

Finally, we also followed the cycling test parameters similar to those employed by a commercial LIC device manufacturer (Ultimo ^{TM}), which are listed on their website[96]. As shown in Figure 5F, the devices were tested for 100,000 cycles between 1.5-3.5 V (51.2 Ag^{-1}), both at 25°C and at 65°C. Our NICs achieved energy/power densities of 8-20 Wh kg^{-1} at ~50000 Wkg^{-1} (active material normalized), retaining 88% and 78% of their capacity after 100,000 cycles at 25 and 65°C. Figure S18 shows the cycling stability of PSNC-3-800//PSOC-A NIC at a current density of

100Ag^{-1} and a voltage window of 2.2-3.8V, which are the current density and voltage window quoted in ref. 96. After 100,000 cycles our NICs capacity degraded by only 1.2%. These values are fully competitive with Ultimo LICs according to the information provided on the manufacturer website. Once again this highlights the attractiveness of our approach considering that our electrode materials are fabricated from waste peanut shells and hence to use the expression "cost peanuts", run on Na rather than on Li, and should be further improvable with industrial-style engineering optimization (electrode fabrication process, electrolyte component adjustment, *etc.*).

Conclusions

To summarize, we created a high performance hybrid sodium ion capacitor (NIC) with the active materials in both electrodes being approximately balanced in their capacity and derived entirely from a single precursor of biomass waste peanut shells. The device offers some of the most promising energy-power-cycling stability combinations reported in literature for either Na or Li ion hybrid systems.

Acknowledgements

This work was sponsored by NSERC Discovery.

Experimental Section

Materials

We employed shells from the peanuts grown and roasted in the Shandong region of China, bags of which the author (HW) gave to the research group as a going away gift. The obtained biomass was firstly soaked in ethanol for 2 weeks, and then washed with MQ-water (Ultrapure water with 18.2 MΩ·cm at 25 °C obtained in Milli-Q water purifier system, Millipore Corporation) and thoroughly dried before use. Rough grinding was used to separate the inner from the outer peanut shell. The PSNC cathode materials were synthesized as follows: A ratio of 1.5 g of outer shell, 2.5 mL of concentrated sulfuric acid and 50 mL of MQ-water were sealed in a 100 mL stainless steel autoclave. The autoclave was heated at 180°C for 48 h and then cooled down naturally. The resulting biochar was collected by filtration, washed with MQ-water and then dried. The yield of biochar is approximately 0.8 g. The dried biochar and activation agent (KOH), in a mass ratio of 1:2 or 1:3, were thoroughly ground and mixed using an agate mortar and pestle. Activation was carried out in a tubular furnace at 800 or 850 °C for 1h under argon flow. The activated samples were thoroughly washed with 2M HCl and MQ-water, and finally dried in an oven at 100°C overnight. The final yield of the PSNC carbons was in the 19 - 29% range (based on the weight of the biochar). The PSOC anode materials were synthesized as follows: A mass of 2g of the inner shell carbonized in argon at 1200°C for 6 h. This resulted in a yield of approximately 0.7 g, i.e. 35%. To remove impurities the obtained carbon was thoroughly washed using 20% KOH at 70°C for 2h, and 2M HCl at 60°C for 15 h, followed by MQ-water. Activation for the PSOC-A was performed at 300°C for 9 h with dry air flown at 50 sccm min^{-1}. The activated carbons were then washed again using the above procedure.

Material Characterization

The surface area and porous texture of carbon materials are characterized by nitrogen adsorption at 77 K (Quantachrome Autosorb^{-1}). Prior to the gas sorption measurements, the samples were outgassed at 250 °C for 4 h under a vacuum. The pore size distribution (PSD) being calculated using density functional theory (DFT) model from the adsorption branch. The pore size distributions were evaluated by a nonlocal DFT method using nitrogen adsorption data and assuming slit-pore geometry. To characterize the morphology of the carbon samples, field emission scanning electron microscopy (FE-SEM) (Hitachi S-4800) and transmission electron microscopy (TEM) (JEOL 2200FS, 200 kV) are used. Low loss electron energy loss spectroscopy (EELS) was performed with scanning TEM (STEM) mode with a nominal electron beam size of 0.5nm. The carbon compact's electrical conductivity was measured using Pro4 from Lucas Laboratories. X-ray photoelectron spectroscopy (XPS) measurements are performed on an ULTRA (Kratos Analytical) spectrometer using monochromatic Al-K_α radiation ($h\upsilon$= 1486.6 eV) run at 210 W. Before XPS analysis, the samples were dried at 110 °C in vacuum oven overnight to remove the absorbed water. X-ray diffraction (XRD) analysis was performed using a Bruker AXS D8 Discover diffractometer with the Cu Kα radiation. The Raman spectra were recorded with a confocal microprobe Raman system (Thermo Nicolet Almega XR Raman Microscope).

Electrochemical Testing

All the electrodes were prepared by coating electrodes slurries (75 wt% active material, 15 wt% carbon black, and 10 wt% polyvinylidenediflouride dissolved in *N*-methylpyrrolidone) on stainless steel spacers, and then dried at 120°C under vacuum overnight. The typical mass loading of the electrodes was 0.4 mg cm^{-2} and each electrode has area of 1.77cm^2. To ensure that this mass loading was adequate for representing the electrochemical performance of a higher loaded electrode, additional testing was performed on both the cathodes and the anodes loaded with 2 mg cm^{-2}. Commercial mass loading electrodes (15 mg cm^{-2}) were prepared identically but pressed at 100 MPa in the final step. Half cells were constructed using standard 2032 button cells, with Na metal as the counter electrode, a polyethene-based separator, and 1M $NaClO_4$ in 1:1 (volume ratio) ethylene carbonate (EC): die1thyl carbonate (DEC) as the electrolyte. Button cell - based Na-ion capacitor (NIC) devices were constructed using opposing carbon electrodes with the same separator and electrolyte. All the cell fabrication and disassembly was performed inside an Ar filled glove box with sub-0.1 ppm water and oxygen contents. To confirm that passivation of Na metal was avoided we cycled Na-Na cells. As shown in Figure S21, there is no degradation of Na-Na cell during the tested 5,000 cycles. Galvanostatic charge/discharge profiles were performed using the BT2000 Arbin electrochemical workstation. Cycling voltammetry and electrochemical impedance spectroscopy (EIS) measurements performed using a Solartron 1470 Multistat system.

References

1 M. D. Slater, D. Kim, E. Lee and C. S. Johnson, *Adv. Funct. Mater.*, 2013, **23**, 947-958.

2 V. Palomares, P. Serras, I. Villaluenga, K. B. Hueso, J. Carretero-Gonzalez and T. Rojo, *Energy Environ. Sci.*, 2012, **5**, 5884-5901.

3 L. Ji, M. Gu, Y. Shao, X. Li, M. H. Engelhard, B. W. Arey, W. Wang, Z. Nie, J. Xiao, C. Wang, J. Zhang and J. Liu, *Adv. Mater.*, 2014, **26**, 2901-2908.

4 J. F. Qian, Y. Xiong, Y. L. Cao, X. P. Ai, H. X. Yang, *Nano Lett*. 2014, **14**, 1865-1869.

5 Y. Wen, K. He, Y. Zhu, F. Han, Y. Xu, I. Matsuda, Y. Ishii, J. Cumings and C. Wang, *Nat. Commun.*, 2014, **5**, 4033.

6 D. Datta, J. W. Li and V. B. Shenoy, *ACS Appl. Mater. Inter.*, 2014, **6**, 1788-1795.

7 H. L. Zhu, Z. Jia, Y. C. Chen, N. Weadock, J. Y. Wan, O. Vaaland, X. G. Han, T. Li and L. B. Hu, *Nano Lett.*, 2013, **13**, 3093-3100.

8 W. Luo, J. Schardt, C. Bommier, B. Wang, J. Razink, J. Simonsen and X. L. Ji, *J. Mater. Chem. A*, 2013, **1**, 10662-10666.

9 C. D. Wessells, M. T. McDowell, S. V. Peddada, M. Pasta, R. A. Huggins and Y. Cui, *ACS Nano*, 2012, **6**, 1688-1694.

10 Y. L. Cao, L. F. Xiao, M. L. Sushko, W. Wang, B. Schwenzer, J. Xiao, Z. M. Nie, L. V. Saraf, Z. G. Yang and J. Liu, *Nano Lett.*, 2012, **12**, 3783-3787.

11 C. Bommier, W. Luo, W. Gao, A. Greaney, S. Ma and X. Ji, *Carbon*, 2014, 76, 165-174.

12 T. H. Hwang, D. S. Jung, J. S. Kim, B. G. Kim and J. W. Choi, *Nano Lett.*, 2013, **13**, 4532-4538.

13 Y. Y. Shao, J. Xiao, W. Wang, M. Engelhard, X. L. Chen, Z. M. Nie, M. Gu, L. V. Saraf, G. Exarhos, J. G. Zhang and J. Liu, *Nano Lett.*, 2013, **13**, 3909-3914.

14 D. W. Su and G. X. Wang, *ACS Nano*, 2013, **7**, 11218-11226.

15 Y. Liu, F. Fan, J. Wang, Y. Liu, H. Chen, K. L. Jungjohann, Y. Xu, Y. Zhou, D. Bigio, T. Zhu and C. Wang, *Nano Lett.*, 2014, **14**, 3445-3452

16 L. J. Fu, K. Tang, K. P. Song, P. A. van Aken, Y. Yu and J. Maier, *Nanoscale*, 2014, **6**, 1384-1389.

17 B. R. Liu, P. Soares, C. Checkles, Y. Zhao and G. H. Yu, *Nano Lett.*, 2013, **13**, 3414-3419.

18 Y. J. Gong, S. B. Yang, L. Zhan, L. L. Ma, R. Vajtai and P. M. Ajayan, *Adv. Funct. Mater.*, 2014, **24**, 125-130.

19 S. M. Oh, S. T. Myung, C. S. Yoon, J. Liu, J. Hassoun, B. Scrosati, K. Amine, Y. K. Sun. *Nano Lett.,* 2014, **14**, 1620-1626.

20 R. Mukherjee, R. Krishnan, T. M. Lu and N. Koratkar, *Nano Energy*, 2012, **1**, 518-533.

21 C. B. Zhu, K. P. Song, P. A. van Aken, J. Maier and Y. Yu, *Nano Lett.*, 2014, **14**, 2175-2180.

22 C. Z. Wu, X. L. Lu, L. L. Peng, K. Xu, X. Peng, J. L. Huang, G. H. Yu and Y. Xie, *Nat. Commun.*, 2013, **4**, 2431.

23 J. X. Zhu, L. J. Cao, Y. S. Wu, Y. J. Gong, Z. Liu, H. E. Hoster, Y. H. Zhang, S. T. Zhang, S. B. Yang, Q. Y. Yan, P. M. Ajayan, R. Vajtai, *Nano Lett.,* 2013, **13**, 5408-5413.

24 C. H. Xu, B. H. Xu, Y. Gu, Z. G. Xiong, J. Sun and X. S. Zhao, *Energy Environ. Sci.*, 2013, **6**, 1388-1414.

25 J. Han, L. L. Zhang, S. Lee, J. Oh, K. S. Lee, J. R. Potts, J. Y. Ji, X. Zhao, R. S. Ruoff and S. Park, *ACS Nano*, 2013, **7**, 19-26.

26 W. Luo, B. Wang, C. G. Heron, M. J. Allen, J. Morre, C. S. Maier, W. F. Stickle and X. L. Ji, *Nano Lett.*, 2014, **14**, 2225-2229.

27 L. Qie, W. M. Chen, H. H. Xu, X. Q. Xiong, Y. Jiang, F. Zou, X. L. Hu, Y. Xin, Z. L. Zhang and Y. H. Huang, *Energy Environ. Sci.*, 2013, **6**, 2497-2504.

28 S. Boukhalfa, D. Gordon, L. L. He, Y. B. Melnichenko, N. Nitta, A. Magasinski and G. Yushin, *ACS Nano*, 2014, **8**, 2495-2503.

29 M. R. Lukatskaya, O. Mashtalir, C. E. Ren, Y. Dall'Agnese, P. Rozier, P. L. Taberna, M. Naguib, P. Simon, M. W. Barsoum and Y. Gogotsi, *Science*, 2013, **341**, 1502-1505.

30 L. Wei, M. Sevilla, A. B. Fuertes, R. Mokaya and G. Yushin, *Adv. Energy Mater.*, 2011, **1**, 356-361.

31 W. J. Qian, F. X. Sun, Y. H. Xu, L. H. Qiu, C. H. Liu, S. D. Wang and F. Yan, *Energy Environ. Sci.*, 2014, **7**, 379-386.

32 L. L. Peng, X. Peng, B. R. Liu, C. Z. Wu, Y. Xie and G. H. Yu, *Nano Lett.*, 2013, **13**, 2151-2157.

33 Z. Li, L. Zhang, B. S. Amirkhiz, X. H. Tan, Z. W. Xu, H. L. Wang, B. C. Olsen, C. M. B. Holt and D. Mitlin, *Adv. Energy Mater.*, 2012, **2**, 431-437.

34 M. Ghaffari, Y. Zhou, H. P. Xu, M. R. Lin, T. Y. Kim, R. S. Ruoff and Q. M. Zhang, *Adv. Mater.*, 2013, **25**, 4879-4885.

35 N. S. Choi, Z. H. Chen, S. A. Freunberger, X. L. Ji, Y. K. Sun, K. Amine, G. Yushin, L. F. Nazar, J. Cho and P. G. Bruce, *Angew. Chem., Int. Edit.*, 2012, **51**, 9994-10024.

36 P. Simon, Y. Gogotsi and B. Dunn, *Science*, 2014, **343**, 1210-1211.

37 K. Naoi, S. Ishimoto, J. Miyamoto and W. Naoi, *Energy Environ. Sci.*, 2012, **5**, 9363-9373.

38 Z. Chen, V. Augustyn, X. L. Jia, Q. F. Xiao, B. Dunn and Y. F. Lu, *ACS Nano*, 2012, **6**, 4319-4327.

39 F. Zhang, T. F. Zhang, X. Yang, L. Zhang, K. Leng, Y. Huang and Y. S. Chen, *Energy Environ. Sci.*, 2013, **6**, 1623-1632.

40 M. Schroeder, M. Winter, S. Passerini and A. Balducci, *J. Power Sources*, 2013, **238**, 388-394.

41 Q. Wang, Z. H. Wen and J. H. Li, *Adv. Funct. Mater.*, 2006, **16**, 2141-2146.

42 H. Kim, M. Y. Cho, M. H. Kim, K. Y. Park, H. Gwon, Y. Lee, K. C. Roh and K. Kang, *Adv. Energy Mater.*, 2013, **3**, 1500-1506.

43 J. Yin, L. Qi and H. Y. Wang, *ACS Appl. Mater. Inter.*, 2012, **4**, 2762-2768.

44 H. L. Wang, Z. W. Xu, Z. Li, K. Cui, J. Ding, A. Kohandehghan, X. H. Tan, B. Zahiri, B. C. Olsen, C. M. B. Holt and D. Mitlin, *Nano Lett.*, 2014, **14**, 1987-1994.

45 R. Ding, L. Qi and H. Wang, *Electrochim. Acta*, 2013, **114**, 726-735.

46 Z. Chen, Y. Yuan, H. H. Zhou, X. L. Wang, Z. H. Gan, F. S. Wang and Y. F. Lu, *Adv. Mater*, 2014, **26**, 339-345.

47 A. Jain, V. Aravindan, S. Jayaraman, P. S. Kumar, R. Balasubramanian, S.

Ramakrishna, S. Madhavi and M. P. Srinivasan, *Sci. Rep.*, 2013, **3**,3002.

48 H. S. Choi, J. H. Im, T. Kim, J. H. Park and C. R. Park, *J. Mater. Chem.*, 2012, **22**, 16986-16993.

49 J. Ding, H. L. Wang, Z. Li, A. Kohandehghan, K. Cui, Z. W. Xu, B. Zahiri, X. H. Tan, E. M. Lotfabad, B. C. Olsen and D. Mitlin, *ACS Nano*, 2013, **7**, 11004-11015.

50 N. Yabuuchi, M. Kajiyama, J. Iwatate, H. Nishikawa, S. Hitomi, R. Okuyama, R. Usui, Y. Yamada and S. Komaba, *Nat. Mater.*, 2012, **11**, 512-517.

51 V. Khomenko, E. Raymundo-Pinero and F. Beguin, *J. Power Sources*, 2008, **177**, 643-651.

52 J. H. Kim, J. S. Kim, Y. G. Lim, J. G. Lee and Y. J. Kim, *J. Power Sources*, 2011, **196**, 10490-10495.

53 B. Hu, K. Wang, L. H. Wu, S. H. Yu, M. Antonietti and M. M. Titirici, *Adv. Mater.*, 2010, **22**, 813-828.

54 Z. Gui, H. L. Zhu, E. Gillette, X. G. Han, G. W. Rubloff, L. B. Hu and S. B. Lee, *ACS Nano*, 2013, **7**, 6037-6046.

55 L. Wei and G. Yushin, *Nano Energy*, 2012, **1**, 552-565.

56 N. A. Liu, K. F. Huo, M. T. McDowell, J. Zhao and Y. Cui, *Sci. Rep.*, 2013, **3**,1919.

57 S. Dutta, A. Bhaumik and C. W. Wu, *Energy Environ. Sci.*, 2014, 10.1039/C4EE01075B.

58 R. J. White, V. Budarin, R. Luque, J. H. Clark and D. J. Macquarrie, *Chem. Soc. Rev.*, 2009, **38**, 3401-3418.

59 M. Latorre-Sanchez, A. Primo and H. Garcia, *Angew. Chem., Int. Edit.*, 2013, **52**, 11813-11816.

60 L. Sun, C. G. Tian, M. T. Li, X. Y. Meng, L. Wang, R. H. Wang, J. Yin and H. G. Fu, *J. Mater. Chem. A*, 2013, **1**, 6462-6470.

61 M. Biswal, A. Banerjee, M. Deo and S. Ogale, *Energy Environ. Sci.*, 2013, **6**, 1249-1259.

62 K. Wilson, H. Yang, C. W. Seo and W. E. Marshall, *Bioresource Technol.*, 2006, **97**, 2266-2270.

63 X. Y. Zhao, J. Chen and F. L. Du, *J. Food Sci. Tech. Mys.*, 2012, **49**, 521-529.

64 A. S. Chang, A. Sreedharan and K. R. Schneider, *Food Control*, 2013, **32**,

296-303.

65 E. I. El-Shafey, *J. Environ. Manage*, 2007, **84**, 620-627.

66 Z. A. Al-Othman, R. Ali and M. Naushad, *Chem. Eng. J.*, 2012, **184**, 238-247.

67 X. J. He, P. H. Ling, J. S. Qiu, M. X. Yu, X. Y. Zhang, C. Yu and M. D. Zheng, *J. Power Sources*, 2013, **240**, 109-113.

68 P. Z. Guo, Q. Q. Ji, L. L. Zhang, S. Y. Zhao and X. S. Zhao, *Acta. Phys-Chim. Sin.*, 2011, **27**, 2836-2840.

69 G. T. K. Fey, Y. Y. Lin, K. P. Huang, Y. C. Lin, T. P. Kumar, Y. D. Cho and H. M. Kao, *Adv. Mater. Res.*, 2012, **415-417**, 1572-1585.

70 I. Watanabe, T. Doi, J. I. Yamaki, Y. Y. Lin and G. T. K. Fey, *J. Power Sources*, 2008, **176**, 347-352.

71 M. Ahmad, S. S. Lee, X. Dou, D. Mohan, J. K. Sung, J. E. Yang and Y. S. Ok, *Bioresour Technol.*, 2012, **118**, 536-544.

72 Z. Y. Zhong, Q. Yang, X. M. Li, K. Luo, Y. Liu and G. M. Zeng, *Ind. Crop. Prod.*, 2012, **37**, 178-185.

73 X. D. Zhang, M. Xu, R. F. Sun and L. Sun, *J. Eng. Gas Turb. Power*, 2006, **128**, 493-496.

74 H. Wang, Z. W. Xu, A. Kohandehghan, Z. Li, K. Cui, X. H. Tan, T. J. Stephenson, C. K. King'ondu, C. M. B. Holt, B. C. Olsen, J. K. Tak, D. Harfield, A. O. Anyia and D. Mitlin, *ACS Nano*, 2013, **7**, 5131-5141.

75 Y. H. Liu, J. S. Xue, T. Zheng and J. R. Dahn, *Carbon*, 1996, **34**, 193-200.

76 C. Y. Su, Y. P. Xu, W. J. Zhang, J. W. Zhao, X. H. Tang, C. H. Tsai and L. J. Li, *Chem. Mater.*, 2009, **21**, 5674-5680.

77 C. Vidal-Abarca, P. Lavela, J. L. Tirado, A. V. Chadwick, M. Alfredsson and E. Kelder, *J. Power Sources*, 2012, **197**, 314-318.

78 A. Bhide, J. Hofmann, A. K. Durr, J. Janek and P. Adelhelm, *Phys. Chem. Chem. Phys.*, 2014, **16**, 1987-1998.

79 V. Augustyn, J. Come, M. A. Lowe, J. W. Kim, P. L. Taberna, S. H. Tolbert, H. D. Abruna, P. Simon and B. Dunn, *Nat. Mater.*, 2013, **12**, 518-522.

80 H. Kim, Y. U. Park, K. Y. Park, H. D. Lim, J. Hong and K. Kang, *Nano Energy*, 2014, **4**, 97-104.

81 S. Y. Kim, J. Hong, R. Kavian, S. W. Lee, M. N. Hyder, Y. Shao-Horn and P. T.

Hammond, *Energy Environ. Sci.*, 2013, **6**, 888-897.

82 S. H. Ha, Y. S. Jeong and Y. J. Lee, *ACS Appl. Mater. Inter.*, 2013, **5**, 12295-12303.

83 H. Kim, H. D. Lim, S. W. Kim, J. Hong, D. H. Seo, D. C. Kim, S. Jeon, S. Park and K. Kang, *Sci. Rep.*, 2013, **3**,1506.

84 M. N. Hyder, S. W. Lee, F. C. Cebeci, D. J. Schmidt, Y. Shao-Horn and P. T. Hammond, *ACS Nano*, 2011, **5**, 8552-8561.

85 S. W. Lee, N. Yabuuchi, B. M. Gallant, S. Chen, B. S. Kim, P. T. Hammond and Y. Shao-Horn, *Nat. Nanotechnol.*, 2010, **5**, 531-537.

86 W. T. Gu, N. Peters and G. Yushin, *Carbon*, 2013, **53**, 292-301.

87 F. Y. Tu, S. Q. Liu, T. H. Wu, G. H. Jin and C. Y. Pan, *Powder Technol.*, 2014, **253**, 580-583.

88 H. R. Byon, B. M. Gallant, S. W. Lee and Y. Shao-Horn, *Adv. Funct. Mater.*, 2013, **23**, 1037-1045.

89 S. W. Lee, B. M. Gallant, Y. Lee, N. Yoshida, D. Y. Kim, Y. Yamada, S. Noda, A. Yamada and Y. Shao-Horn, *Energy Environ. Sci.*, 2012, **5**, 5437-5444.

90 R. Mukherjee, A. V. Thomas, D. Datta, E. Singh, J. W. Li, O. Eksik, V. B. Shenoy and N. Koratkar, *Nat. Commun.*, 2014, **5**,3710.

91 H. G. Wang, Z. Wu, F. L. Meng, D. L. Ma, X. L. Huang, L. M. Wang and X. B. Zhang, *ChemsusChem*, 2013, **6**, 56-60.

92 K. Tang, L. J. Fu, R. J. White, L. H. Yu, M. M. Titirici, M. Antonietti and J. Maier, *Adv. Energy Mater.*, 2012, **2**, 873-877.

93 X. Zhou, Y. G. Guo, *ChemElectroChem*, 2014, **1**, 83–86.

94 A. Ponrouch, A. R. Goni and M. R. Palacin, *Electrochem Commun.*, 2013, **27**, 85-88.

95 V. G. Pol, E. Lee, D. H. Zhou, F. Dogan, J. M. Calderon-Moreno and C. S. Johnson, *Electrochim. Acta*, 2014, **127**, 61-67.

96 http://www.jmenergy.co.jp/en/products_cell_can.html

97 Y. Gogotsi, P. Simon, *Science*, 2011, **334**, 917-918.

98 Y. W. Zhu, S. Murali, M. D. Stoller, K. J. Ganesh, W. W. Cai, P. J. Ferreira, A. Pirkle, R. M. Wallace, K. A. Cychosz, M. tommes, D. Su, E. A. Stach, R. S. Ruoff, *Science*, 2011, **332**, 1537-1541.

99 http://www.jsrmicro.com/index.php/EnergyAndEnvironment

100 H. Wang, C. M. Holt, Z. Li, X. Tan, B. S. Amirkhiz, Z. Xu, B. Olsen, T. Stephenson, D. Mitlin, *Nano Res*., 2012, **5**, 605-617.

101 W. Wei, X. Cui, W. Chen, D. Ivey, *Chem. Soc. Rev.*, 2011, **40**, 1697-1721.

102 D. Cericola, R. Kotz, *Electrochim. Acta*, 2012, **72**, 1-17.

103 G. Wang, L. Zhang, J. Zhang, *Chem. Soc. Rev.*, 2012, **41**, 797-828.

104 K. Leng, F. Zhang, L. Zhang, T. F. Zhang, Y. P. Wu, Y. H. Lu, Y. Huang and Y. S. Chen, *Nano Res.*, 2013, **6**, 581-592.

105 X. Zhao, L. L. Zhang, S. Murali, M. D. Stoller, Q. H. Zhang, Y. W. Zhu and R. S. Ruoff, *ACS Nano*, 2012, **6**, 5404-5412.

106 J. Yan, Z. J. Fan, W. Sun, G. Q. Ning, T. Wei, Q. Zhang, R. F. Zhang, L. J. Zhi and F. Wei, *Adv. Funct. Mater.*, 2012, **22**, 2632-2641.

107 S. Shi, C. J. Xu, C. Yang, Y. Y. Chen, J. J. Liu and F. Y. Kang, *Sci. Rep.*, 2013, **3**,2598.

108 C. G. Liu, Z. N. Yu, D. Neff, A. Zhamu and B. Z. Jang, *Nano Lett.*, 2010, **10**, 4863-4868.

109 Z. Chen, V. Augustyn, J. Wen, Y. W. Zhang, M. Q. Shen, B. Dunn and Y. F. Lu, *Adv. Mater*, 2011, **23**, 791-795.